



Characterization of As-Welded Microstructure in a P91 Steel

MX precipitate identity and the presence of retained austenite are potential factors to consider for Type IV cracking occurrence

BY A. L. MARZOCCA, F. SOLDERA, M. ZALAZAR, C. A. DANÓN, AND M. I. LUPPO

Abstract

The microstructure of the heat affected zone (HAZ) and fusion zone (FZ) in the as-welded condition of a single-pass weld performed by the flux-cored arc welding (FCAW) process was studied in a P91 steel using microhardness measurements, field-emission scanning electron microscopy, transmission electron microscopy, and x-ray diffraction. The evolution of precipitates in each region of the single-pass weld was analyzed, and particular attention was paid to the presence of retained austenite (RA). Experimental observations indicated that $M_{23}C_6$ carbide played a major role in the thermal cycle associated with the weldment. On one hand, the dissolution of $M_{23}C_6$ led to the precipitation of spherical NbCN in the fine-grained HAZ (FGHAZ) near the coarse-grained HAZ (CGHAZ). On the other hand, the total or partial dissolution of $M_{23}C_6$ carbides changed the chemical composition of the initially formed austenite. In the regions where the $M_{23}C_6$ carbides were completely dissolved (i.e., the CGHAZ and FZ), retained austenite was observed as a thin, continuous film along primary austenite grains and lath boundaries. Instead, a shell of retained austenite was observed around some partially dissolved $M_{23}C_6$ of the intercritical HAZ (ICHAZ) and FGHAZ.

Keywords

- 9% Cr Steels
- Welding
- Precipitates
- Retained Austenite
- Electron Microscopy
- X-Ray Diffraction

Introduction

To increase the thermal efficiency of advanced power generation systems, a continuous search for higher operation temperatures and pressures has taken place during the last three decades. Ferritic-martensitic steels of 9Cr1MoNbV Grade 91 (hereafter P91 steel) have been extensively used in conventional power plant components, heat exchangers, piping, and tubing, etc., due to their excellent combination of properties, such as creep resistance, toughness, and resistance to oxidation at high temperatures (Ref. 1). P91 steels are also proposed as the primary option for different structural components for the so-called Generation IV nuclear reactors due to their exceptionally high void swelling resistance (Ref. 2) and very good creep behavior under irradiation.

The manufacturing steps for P91 steel include normalizing at 1050–1060°C (1922–1940°F) and tempering at 750–780°C (1382–1436°F). The resulting microstructure is a lath martensite with a high dislocation density and precipitated phases, such as $M_{23}C_6$ carbides ($M = Cr, Fe, Mo$) and MX carbide-nitrides ($M = V, Nb, Cr; X = C, N$) with face-centered cubic (FCC) crystal structure (Refs. 3–5). Three types of MX particles have been reported after tempering. MX Type I (NbCN) is a spherical Nb-rich precipitate that is observed in every steel air-cooled from normalization at 1100°C (2012°F). MX Type II (VN) is a fine, V-rich MX with a rod or plate shape. MX Type III, or “wings,” represents a specific morphology that is formed by secondary precipitation of VN “wings” adhering to an NbCN core at the tempering stage (Ref. 6).

Welding in all its varieties is still the major joining and repair technology for power plant components. The microstructure of joined materials is strongly influenced by the welding process, and, thereby, their mechanical properties are altered (Ref. 7). As a result of the several thermal cycles caused by the welding process, the microstructure is affected, and a so-called heat-affected zone (HAZ) is formed. The HAZ can be divided into three sub-zones: intercritical zone (ICHAZ), fine-grained zone (FGHAZ), and coarse-grained zone (CGHAZ) (Ref. 8).

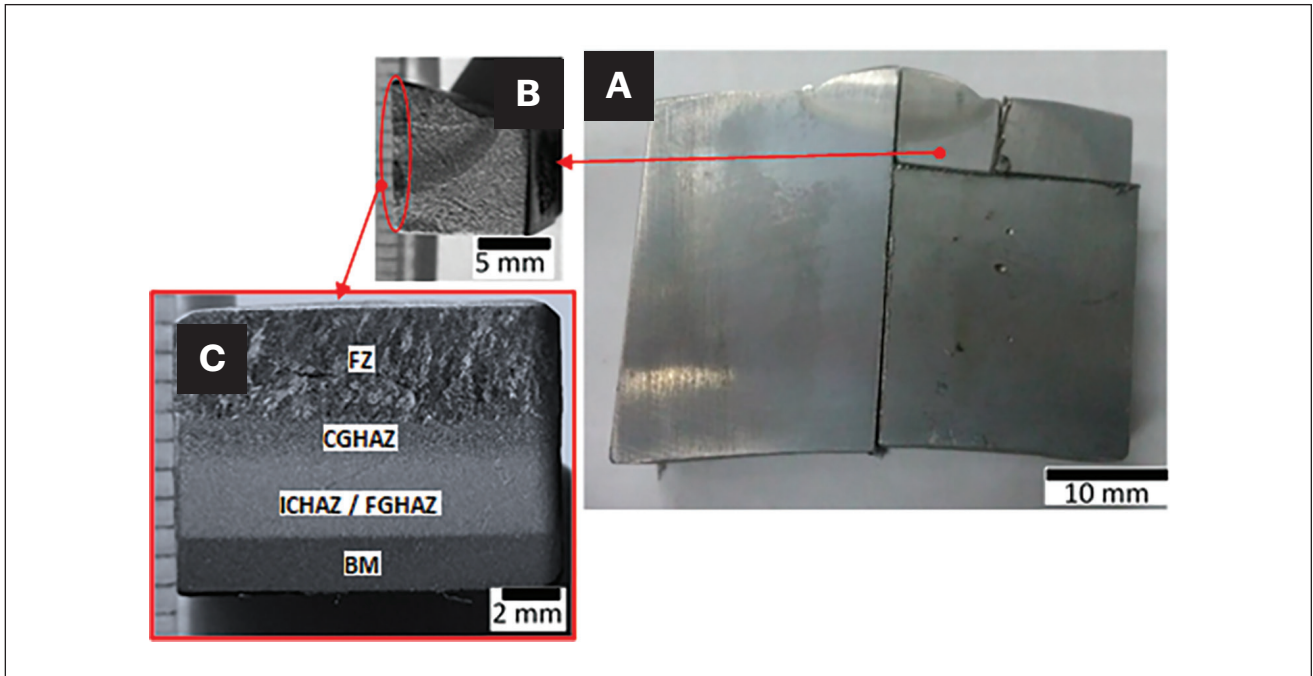


Fig. 1 — Macrograph of the single-pass weld seam showing the different cuts made to study the FZ and HAZ regions: A — Cross-sectional macrograph; B — second cut, following the welding line; C — parallel view of the different subzones of the HAZ.

The high-temperature conditions that martensitic-ferritic 9–12% Cr steels operate under in power stations induce Type IV cracking. This type of cracking occurs in the ICHAZ or FGHAZ via a creep mechanism (Ref. 9). Abe (Ref. 10) carried out creep rupture tests on laboratory HCM12A specimens that had been heated to temperatures in the range of 800 to 1000°C (1472 to 1832°F) to simulate different parts of the HAZ. He reported that while hardness had its minimum value after heating to temperatures near A_{c1} , the creep rupture time in tests carried out at 650°C (1202°F) had its minimum value in specimens heated to temperatures near A_{c3} . From his results, it appears that at high stresses (140 MPa), failure preferentially occurred in specimens heated slightly below the A_{c3} (i.e., intercritically heated), whilst at lower stresses (< 120 MPa), the minima shifted to specimens heated to just beyond the A_{c3} (i.e., the fully transformed fine-grained specimens). This apparent shift in the failure position with stress may explain why both regions of the outer HAZ have been associated with Type IV failure.

The welded joints of P91 steel are generally submitted to postweld heat treatment (PWHT) to optimize the microstructure and to reduce the residual stresses after welding. Therefore, few studies have been focused on the as-welded HAZ microstructure (Refs. 11–14). However, the initial microstructure in the HAZ immediately after welding may be directly responsible for the subsequent structural evolution during the PWHT and for the creep behavior in the high-temperature service life. It is of utmost importance to detect the presence of retained austenite (RA) in the as-welded condition. Indeed, RA could decompose in ferrite, a phase that could alter the strength properties of the material during PWHT. Ferrite is hardly distinguishable from tempered martensite in the PWHT condition; thus, the reason to study the as-welded condition

is to obtain a precise picture of the subsequent location of ferrite after RA decomposition. Unlike multipass welding, where the microstructure is modified owing to reheating effects, a single-pass weld allows the evaluation of the phases present in the sub-zones of the HAZ before they are modified by the next temperature rise. The purpose of this work was to characterize the microstructure of the HAZ in the as-welded condition of a single-pass weld performed by the flu-cored arc welding (FCAW) process for a P91 steel. The microstructural characterization after welding was performed using microhardness measurements, field-emission scanning electron microscopy (FESEM), transmission electron microscopy (TEM), and x-ray diffraction.

Experimental Procedure

Material and Welding Process

A bead-on-pipe single-pass weld was performed in a pipe of P91 steel provided by JFE Corporation, Japan, with a wall thickness of 28.5 mm (1.122 in.) and an outer diameter of 350 mm (13.779 in.). The material was received in the standard metallurgical condition (i.e., normalized at 1050°C, 10 min, and tempered at 785°C (1445°F), 45 min. The chemical composition is shown in Table 1.

The process employed was FCAW under 80%Ar/20%CO₂ gas shielding. The filler material was a rutilic slag wire AWS A5.29/A5.29M:2010 E91T1, whose chemical composition is shown in Table 1.

The welding parameters used were preheat temperature 260°C (500°F); welding voltage 26 V; welding current 160

Table 1 – Chemical Composition of the P91 Steel and E91T1 Filler Material (wt-%)

	C	Mn	Si	Ni	Cr	Mo	Al	Nb	Ti	V
P91	0.107	0.44	0.3	0.17	9.26	0.86	0.004	0.09	0.002	0.21
E91T1	0.103	0.94	0.318	0.48	9.92	0.93	0.003	0.046	0.033	0.25

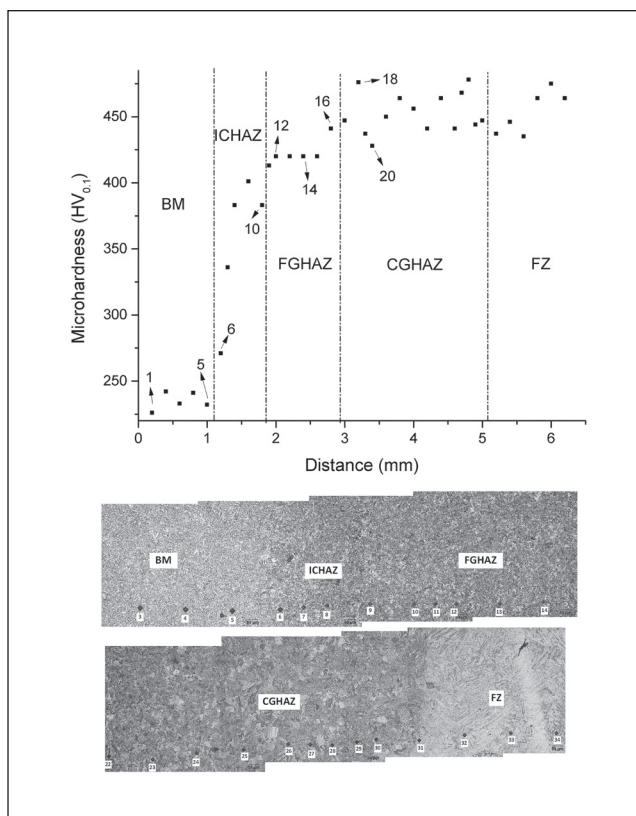


Fig. 2 – Microhardness profile across the single-pass weld.

A; welding speed 3 mm (0.118 in.)/s; welding heat input 1.4 kJ/mm (the indicated heat input values are not affected by thermal efficiency). The weldment was slowly cooled in air. A ceramic blanket was used for cooling, and the cooling process was registered by a series of thermocouples located at different distances of the weld centerline.

Characterization Techniques

The metallographic preparation was carried out by standard polishing down to 1 μm diamond paste and etching with Vilella's reagent. Vickers microhardness profiles were performed using Leitz Durimet equipment with a load of 100 g (3.527 oz). Scanning electron microscopy was carried out with a Zeiss SUPRA™ 40 field emission gun system (FESEM) using an accelerating voltage of 5 kV.

Transmission electron microscopy was carried out with a Philips CM200 microscope equipped with an EDAX-DX4 system for energy dispersive analysis of x-rays (EDS). Two

types of samples were examined: 1) carbon extraction replicas were used to identify the precipitated particles without interference from the ferrous matrix; and 2) thin foils were used to determine the nature of phases present within the matrix. Extractive replicas were prepared by polishing the surface of the samples down to 1 μm diamond cloth, carbon evaporation onto them, and etching with Vilella's reagent. To obtain extractive replicas of a particular subzone of the HAZ, samples were masked except for the selected subzone. Thin foils of the base metal (BM) and fusion zone (FZ) were obtained with a Struers TenuPol-5 jet-electropolishing system. The electrolyte used was a solution of 10% perchloric acid and 90% methanol. The temperature was maintained below -35°C (-31°F).

An FEI Helios 600 dual beam field emission gun scanning electron microscope and ion beam system (FIB-SEM) was used to obtain thin foils of the different subzones within the HAZ (CGHAZ, FGHAZ, and ICHAZ), which were inaccessible regions using the conventional technique. The lift-out technique was used to extract the foils. The milling process was performed with an ion beam (Ga) at 30 kV with different currents (400 pA, 200 pA, 93 pA, and 48 pA). To minimize possible artifacts, such as amorphization and Ga implantation, final milling was done at 5 kV with an ion beam current of 16 pA for approximately 2 min.

X-ray measurements were performed using a Panalytical Empyrean diffractometer with θ - 2θ Bragg-Brentano geometry, a flat graphite monochromator, and Ni-filtered $\text{Cu-K}\alpha$ radiation. The diffracted radiation was collected between 35 and 120 deg (2θ) with an ultra-fast PixCel area detector with a step scan angle settled at 0.026 deg. To detect the presence of austenite, two regions with an area enough to be irradiated were chosen (i.e., the BM and FZ). The FZ was cut to expose the midplane. After polishing down to 1 μm diamond paste, both samples were electrolytically polished at 35 V using a solution of 90% Butyl CELLOSOLVE™ and 10% perchloric acid.

Results

Characterization of Microstructure Evolution by Microhardness Measurements and FESEM Observations

Figure 1 displays a macrograph of the weld seam showing the different cuts that were made to study the fusion zone and the HAZ.

The microhardness profile across the single-pass weld in the P91 steel is reproduced in Fig. 2. A continuous increase

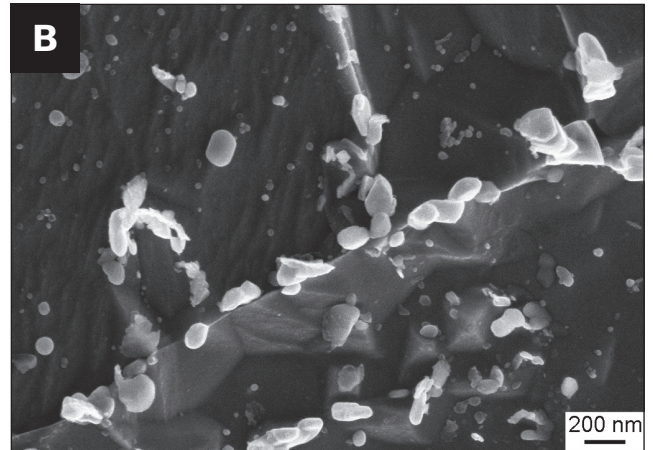
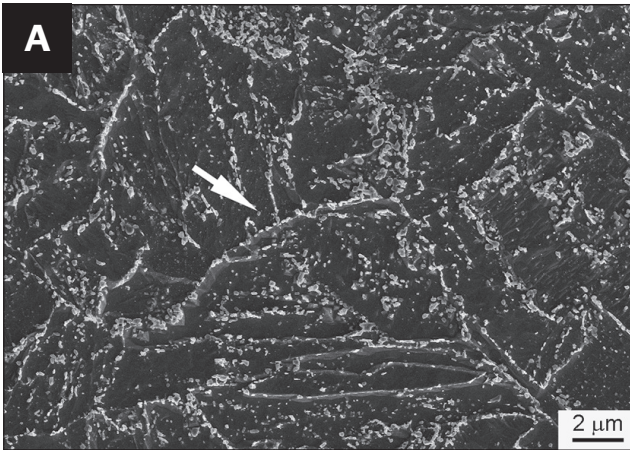


Fig. 3 — FESEM micrographs of the BM: A — General view; B — higher magnification of the arrowed area in (A) where precipitates with two different sizes can be distinguished.

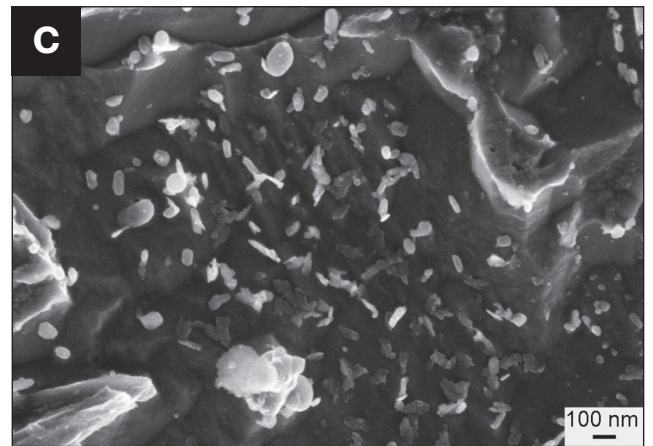
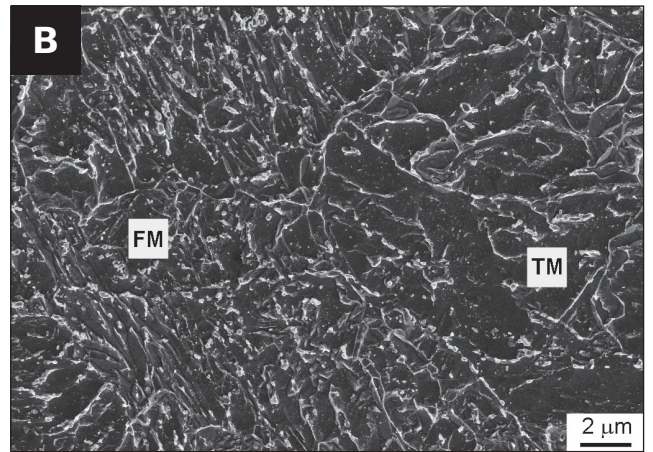
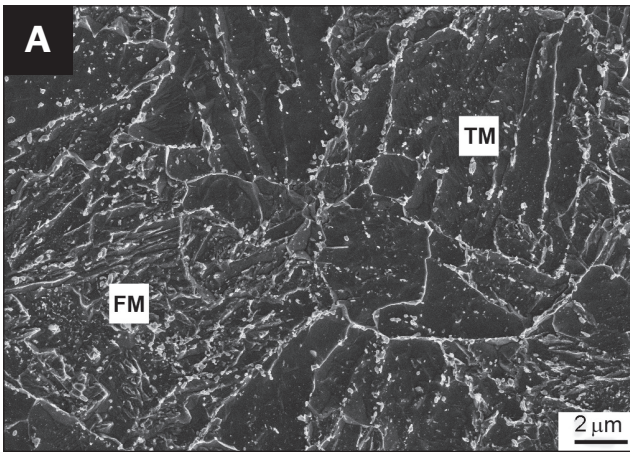


Fig. 4 — FESEM micrographs of the ICHAZ: A — Near indent 6; B — near indent 10; C — precipitates observed in the FM zones where oriented needle-like precipitates can be distinguished. TM: tempered martensite, FM: fresh martensite.

in microhardness from the base material, $(235 \pm 7) \text{HV}_{0.1}$, to the end of the ICHAZ, $(399 \pm 15) \text{HV}_{0.1}$, was observed. In the FGHAZ, the microhardness remained practically constant, $(419 \pm 3) \text{HV}_{0.1}$, and only underwent an increase near the CGHAZ (indent 16). In the CGHAZ and FZ, the hardness was $(453 \pm 15) \text{HV}_{0.1}$.

Figure 3 shows FESEM micrographs of the unaffected BM zone. The microstructure consisted of a tempered lath martensite with the presence of second-phase precipitates of two different sizes. The prior austenite grains (PAGs) had heterogeneous grain size, and their boundaries were decorated mainly by the coarser precipitated particles.

Peak temperatures in the ICHAZ lie between the A_{c1} and A_{c3} transformation temperatures, and a partial transformation from martensite to austenite results in heating. While new austenite grains nucleate at favored positions, like PAG boundaries or martensite lath boundaries, the remaining tempered martensite is simply tempered for a second time by the weld thermal cycle (Ref. 8). Then, two types of martensite can be identified at the end of the cycle: tempered martensite (TM), coming from the as-received material and not transformed into austenite, and fresh martensite (FM), resulting from the cooling of the austenite formed during the transformation in the intercritical range of the P91 steel.

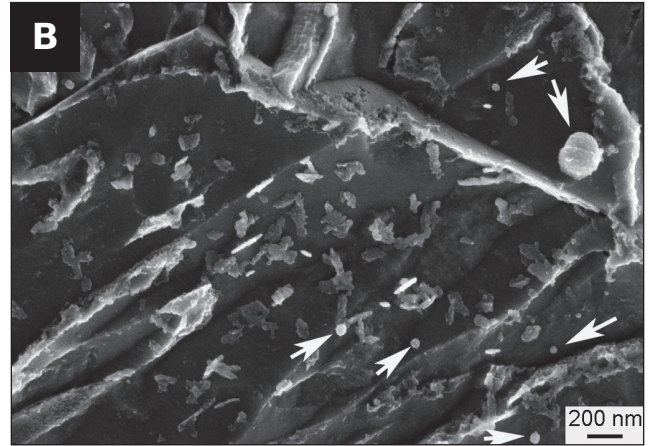
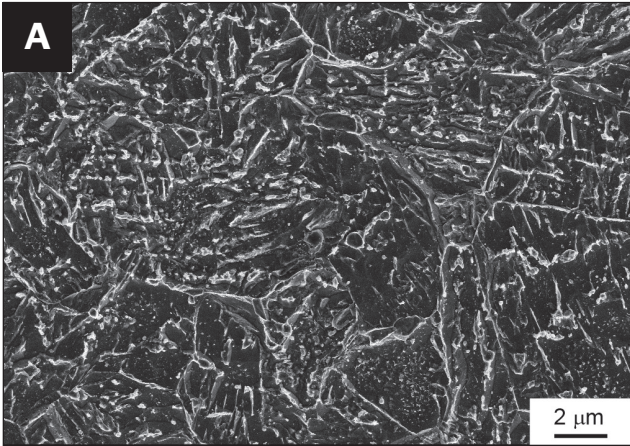


Fig. 5 – FESEM micrographs of the FGHAZ: A – Near indent 14; B – near indent 16. Arrows indicate spherical precipitates with two range sizes.

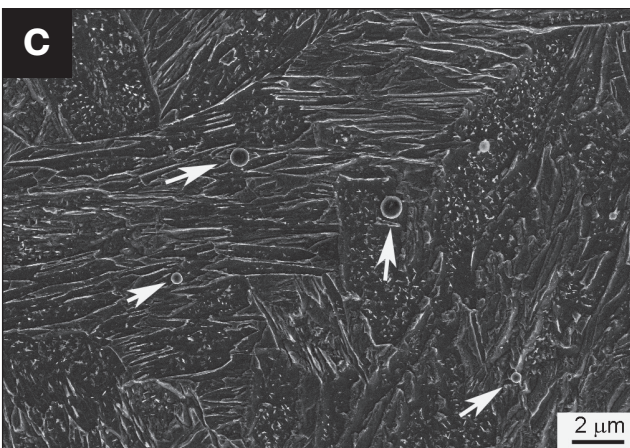
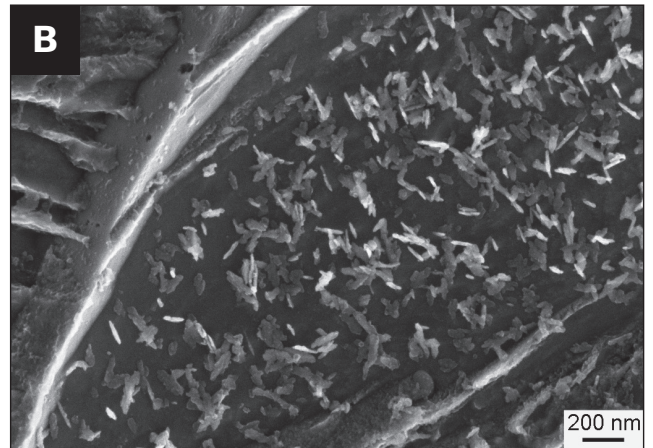
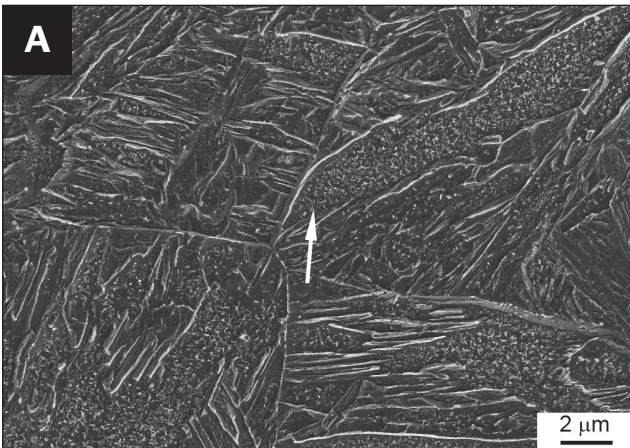


Fig. 6 – FESEM micrographs of the: A – CGHAZ near indent 20; B – higher magnification of the area indicated in (A) where oriented needlelike precipitates can be distinguished; C – FZ where arrows indicate the presence of inclusions.

Figs. 4A and 4B show the microstructure of the ICHAZ near indent 6 and 10, respectively, indicated in Fig. 2. Using FESEM observations, it was possible to recognize the two kinds of martensite employing the criteria used in Ref. 15. In that work, different states of martensite were obtained in a fast dilatometer using the technique of interrupted heating at temperatures within the intercritical range followed by quenching. Comparing the observations by TEM and field emission gun-scanning electron microscopy (FESEM), it was possible to conclude from Ref. 15 that there is a relationship between morphologies and phases (i.e., a smooth, wavy morphology is associated with TM, while a rough morphology accounts for FM). This identification assumes, of course, that the higher the temperature, the greater the amount of austenite produced. Thus, the rough morphology covers most of the region as the peak temperature increases, as can be seen by comparing the microstructure near indent 10 (Fig. 4B) with the microstructure near indent 6 (Fig. 4A). In the TM zones, the precipitates described in Fig. 3B are again distinguished; in the FM zones, needle-shaped precipitates were observed as well (Fig. 4A).

During welding, the FGHAZ is heated into the lower temperatures of the γ -phase field and the peak temperature may be not high enough to dissolve precipitates completely, lim-

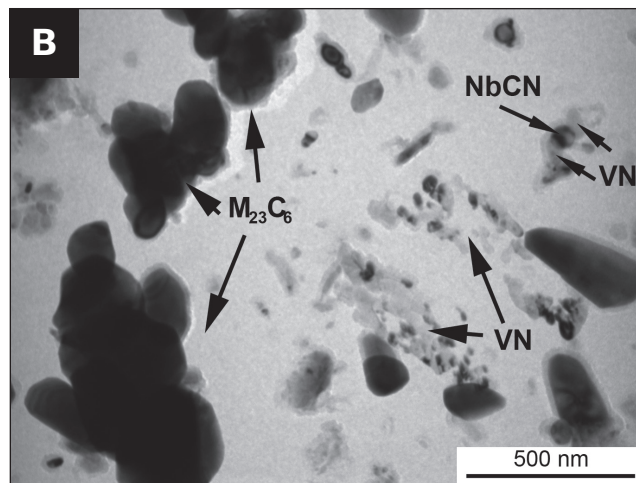
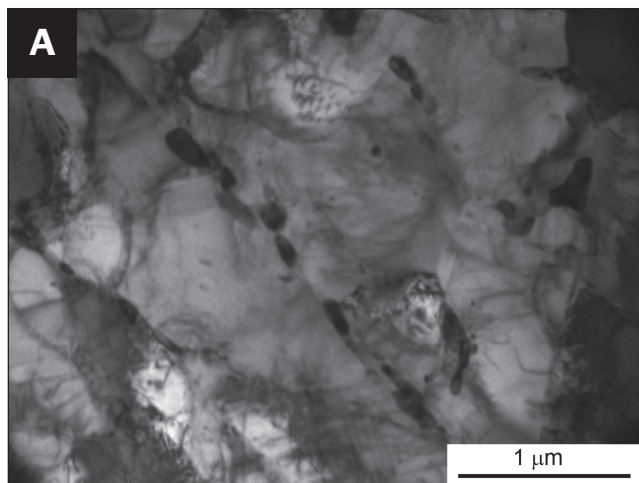


Fig. 7 – TEM micrographs of the BM: A – Tempered lath martensite observed in a thin foil; B – precipitates identified in an extraction replica.

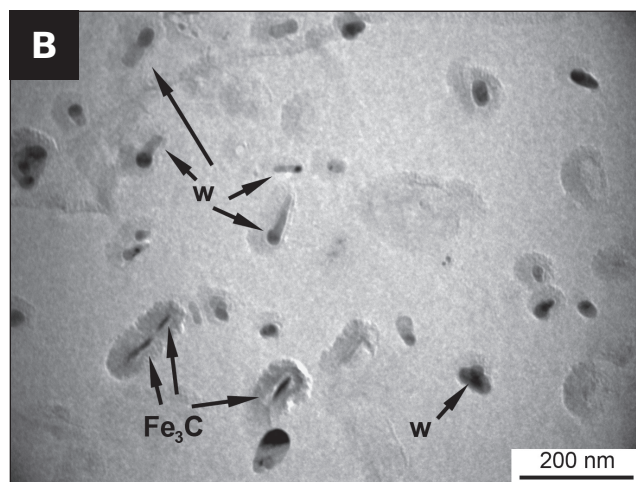
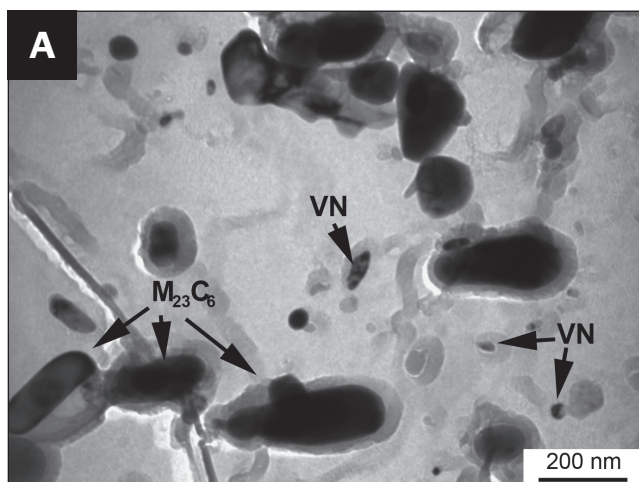


Fig. 8 – TEM micrographs of the ICHAZ (extraction replicas): A – precipitates identified in the TM zones; B – “wings” (*w*) and Fe_3C identified in the FM zones.

iting grain growth by pinning the austenite grain boundaries. On cooling, a fine-grained FM microstructure is formed in the FGHAZ (Fig. 5A). The same types of precipitates observed in the FM zones of the ICHAZ (Fig. 4C) were distinguished near the indents 12 and 14, but in the FGHAZ near the CGHAZ (indent 16), spherical precipitates with two range sizes (indicated by arrows) and needle-shaped precipitates were observed as well (Fig. 5B).

The CGHAZ is heated into the higher temperature region of the γ -phase field during welding, and the original carbide particles are dissolved, resulting in coarse prior austenite grains and martensite laths (Ref. 16). The FESEM micrograph of Fig. 6A shows martensite laths inside the coarse PAGs of the CGHAZ. Needle-shaped precipitates were mainly observed (Fig. 6B); some coarse, spherical precipitates were also distinguished.

The fusion zone (FZ) represents the region that liquefied during welding. The FZ shows columnar grains with many inclusions (Fig. 6C). The inclusions, with varying sizes (0.3–2

μm), are associated with the nature of flux, a rutilic slag wire, AWS A5.29/A5.29M:2010 E91T1, used during the FCAW cycle (Ref. 17). As in the CGHAZ (Fig. 6B), only needlelike precipitates were distinguished in the FZ.

TEM Identification of Precipitates

The microstructure in the BM consists of tempered lath martensite, as shown in Fig. 7A. In a previous work (Ref. 18), the identification of precipitates in the BM was performed using TEM on carbon extraction replicas (Fig. 7B). The $M_{23}C_6$ carbides (crystal structure: cubic; space group: $225 - Fm\bar{3}m$; lattice parameter: $a = 1.063 \text{ nm}$) were the major second phase observed. Thus, particles with low Mo ($M \sim 58Cr-31Fe-9Mo-2V$) and very few with high Mo content ($M \sim 36Cr-41Fe-23Mo$) were present in the BM; despite these composition differences, the electron diffraction pattern confirmed the $M_{23}C_6$ crystal structure in both cases. According to Vijayalakshmi et al. (Ref. 11), the $M_{23}C_6$ phase with high Mo

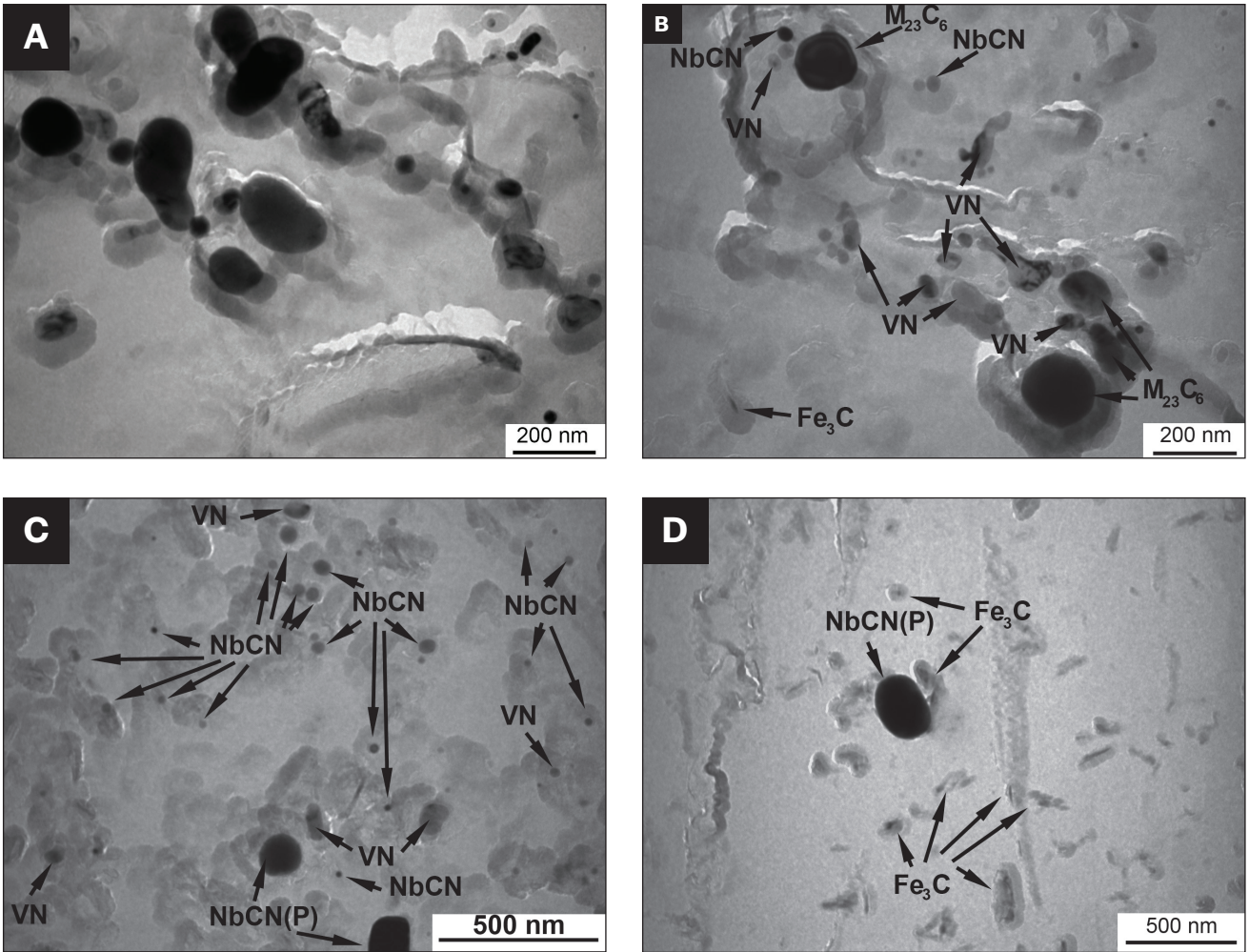


Fig. 9 – TEM micrographs (extraction replica) where the identified precipitates are indicated: A – FGHAZ near ICHAZ; B – FGHAZ intermediate; C – FGHAZ near CGHAZ; D – CGHAZ.

content could have formed at temperatures above 800°C. The next precipitated phase as for the estimated volume fraction was the VN (~55V-23Cr-22Nb) and then the “wings.” The VN phase (crystal structure: cubic; space group: 225 – $Fm\bar{3}m$; lattice parameter: $a = 0.412$ nm) was observed isolated or forming clusters; small spherical NbCN precipitates (crystal structure: cubic; space group: 225 – $Fm\bar{3}m$; lattice parameter: $a = 0.441$ nm) were found as well, in a very low proportion. On the other hand, coarse spherical precipitates with an average chemical composition 67Nb-26V-7Cr (hereafter “primary NbCN,” NbCN (P)) were also identified. Jones et al. (Ref. 19) showed that a water-quenched P91 steel exhibited occasional equiaxed particles, approximately 0.1 to 0.5 μm in diameter, after austenitizing at 1045°C (1913°F); these particles were identified as NbC. The size (coarse when compared to other MX precipitates) and morphology of the NbC particles suggest that they are residual precipitates undissolved during the thermal cycle.

$M_{23}C_6$ was the major precipitate in the TM regions of the ICHAZ (Fig. 8A). Most of the MX particles found in the ICHAZ corresponded to VN isolated precipitates or clusters; then, NbCN and very few “wings” were detected with a lower

volume fraction. At the same time, very few areas with “wings” and Fe_3C precipitates (crystal structure: orthorhombic; space group: 63 – $Pnma$; lattice parameters: $a = 0.5090$ nm, $b = 0.6748$ nm, $c = 0.4523$ nm; average chemical composition of 85Fe-15Cr) were identified, as shown in Fig. 8B. This type of precipitate (needle-shaped) was also observed in the FM zones of the ICHAZ (see Fig. 4C) using FESEM.

TEM micrographs in Figs. 9A–C show the evolution of precipitates in the FGHAZ as the peak temperature increased. Fig. 9A shows a TEM micrograph of the FGHAZ near the ICHAZ where the identified precipitates were the same already present in the ICHAZ with similar chemical compositions. $M_{23}C_6$ carbides were still the major observed precipitates, followed by MX particles in the same order that they appeared in the ICHAZ. In the intermediate region of the FGHAZ (Fig. 9B), the spheroidization of precipitates was observed, and $M_{23}C_6$ carbides, VN, NbCN, and Fe_3C were identified in descending order according to the estimated volume fraction. Near the CGHAZ (Fig. 9C), the FGHAZ showed fine spherical NbCN, a few spherical VN, and Fe_3C . It was possible to observe some coarse NbCN (P).

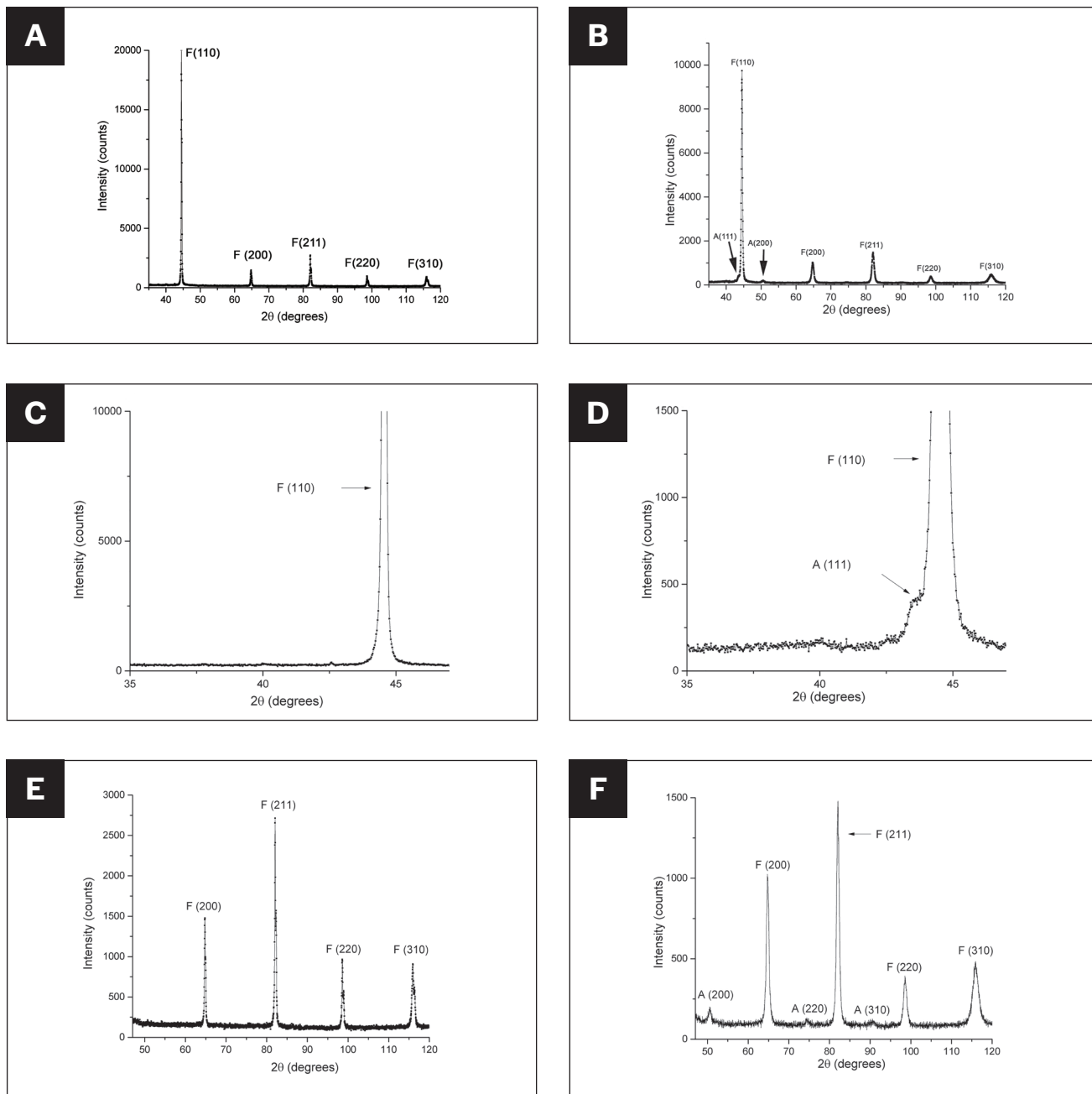


Fig. 10 – X-ray diffraction pattern of the BM (F: ferrite, A: austenite): A – Complete view; C – magnified view from 35 to 47 deg; E – magnified view from 47 to 120 deg. X-ray diffraction pattern of the FZ: B – Complete view; D – magnified view from 35 to 47 deg; F – magnified view from 47 to 120 deg.

The two kinds of precipitates found in the CGHAZ are shown in Fig. 9D: coarse, spherical NbCN (P), and needle-shaped Fe₃C. In the FZ, only needle-shaped Fe₃C precipitates were identified.

Table 2 summarizes the precipitates identified in the BM, HAZ, and FZ of the single-pass weld. NbCN (P) was not considered in Table 2 for these particles; even if they are probably present in all zones except the FZ, they are difficult to find because they are masked by the large amount of M₂₃C₆ carbides having the same morphology and size (Ref. 20).

Identification of Retained Austenite (RA)

To provide additional evidence for the presence of retained austenite after a single-pass welding process, x-ray measurements were performed. Figure 10A displays the x-ray diffraction pattern of the BM; in the magnified views of the 35–47 deg (Fig. 10C) and 47–120 deg (Fig. 10E) angular regions, the identified peaks of tempered martensite (in practice and due to the low carbon content of the steel, ferrite) have been pointed out.

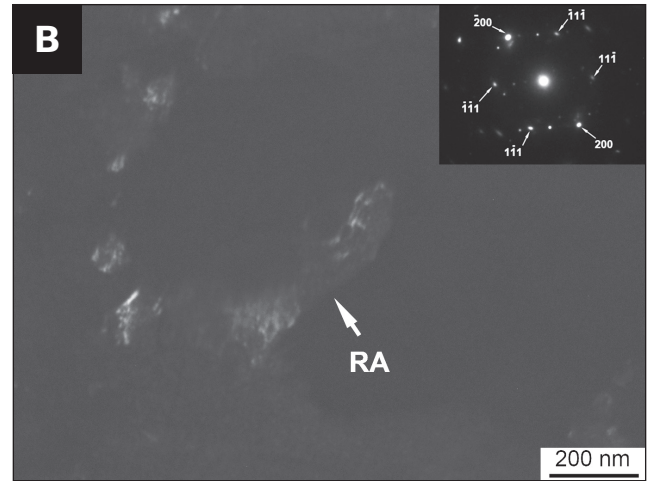
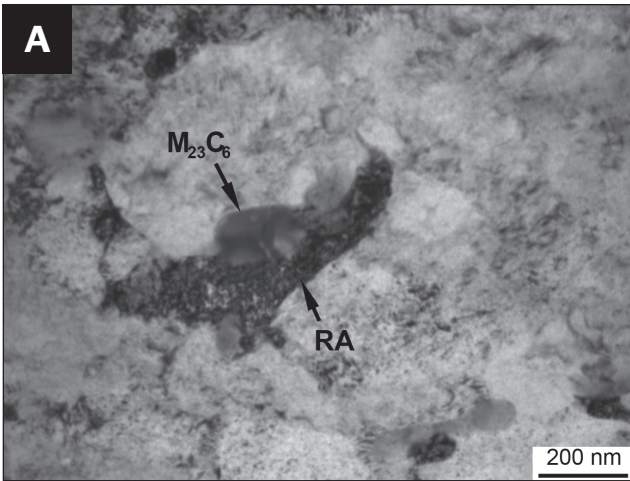


Fig. 11 – A – TEM bright field micrograph (thin foil) of the ICHAZ; B – TEM dark field micrograph corroborating the presence of RA around an undissolved $M_{23}C_6$. At the corner, the SADP of the RA, axis zone $z = [011]\gamma$.

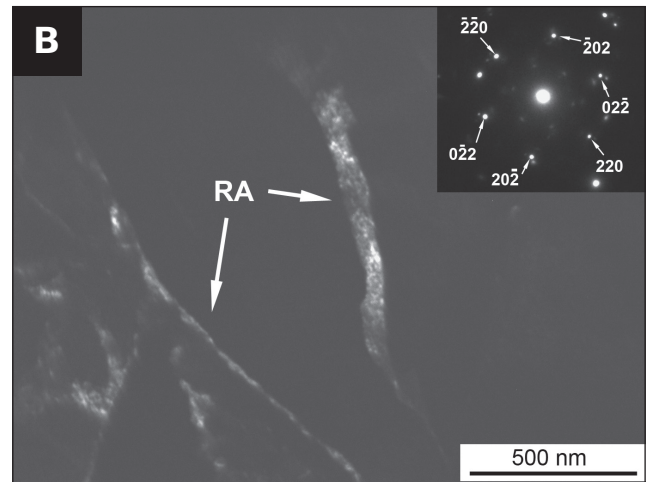
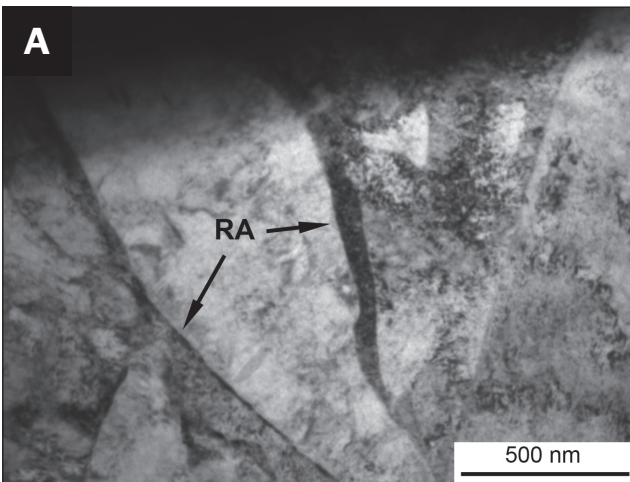


Fig. 12 – A – TEM bright field micrograph (thin foil) of the CGHAZ; B – TEM dark field micrograph showing interlath RA. At the corner, the SADP of the RA, axis zone $z = [111]$.

On the other hand, as the width of the HAZ was very thin (~ 4 mm [0.157 in.]), x-ray diffraction measurements in the FZ could be performed only by doing a crosscut through the midplane of the welding and exposing this area to the beam. The most major detected structure was as-quenched martensite; the comparison between the FZ and BM diffraction patterns evidenced that FZ peaks were broader than the corresponding BM ones, accounting for the finer structure that comes from quenching (Figs. 10B, 10D, and 10F). Besides, retained austenite presence was also determined in the FZ region.

Particular attention was paid to the morphology and distribution of RA. In the ICHAZ and FGHAZ, some $M_{23}C_6$ carbides were found to be partially dissolved and in contact with RA. An example is shown in Fig. 11, which exhibits the bright field and dark field images of such a situation along with the selected area diffraction pattern (SADP) and the indexing for RA (γ phase). The dark field micrograph taken using the spot $(\bar{2}00)_\gamma$ reflection undoubtedly confirms that

this is the fcc γ phase around an undissolved (or partially dissolved) $M_{23}C_6$ carbide.

On the other hand, thin continuous films of retained austenite were observed along PAG boundaries and lath boundaries in the CGHAZ and FZ. The bright and dark field images, the SADP, and its indexing for the RA (γ phase) are shown in Fig. 12. Again, the dark field micrograph taken using the spot $(\bar{2}\bar{2}0)_\gamma$ reflection confirms that this was the fcc γ phase.

Discussion

Microhardness and Microstructural Features

The first evidence of the microstructural variations in the single-pass weld HAZ is given by the microhardness profile. In the ICHAZ, FM coexists with TM; hence, the greater the amount of FM, the higher the microhardness. The low and

Table 2 — Precipitates Identified in the Single-Pass Weld of the P91 Steel

Zone						
	BM		$M_{23}C_6$	VN	“wings”	NbCN
		ICHAZ	$M_{23}C_6$	VN	NbCN	“wings” Fe_3C
		Near ICHAZ	$M_{23}C_6$	VN	NbCN	“wings” Fe_3C
HAZ	FGHAZ	Intermediate	$M_{23}C_6$	VN	NbCN	Fe_3C
		Near CGHAZ	NbCN	VN	Fe_3C	
		CGHAZ	Fe_3C			
	FZ		Fe_3C			

high values of microhardness in the ICHAZ — close to the BM and FGHAZ, respectively — are consistent with the presence of 100% soft TM and 100% hard FM. It is worth noticing that there was no smooth microstructural gradient from the ICHAZ to FGHAZ but a “jump” from presence to absence of TM; in fact, the only subzone of the HAZ that showed the simultaneous presence of FM and TM was the ICHAZ. Indeed, the BM was fully covered by TM, and the FGHAZ, CGHAZ, and FZ displayed a fully FM microstructure. Since the hardness of martensite increases with increasing carbon content, the dissolution of carbide particles in the austenite of the CGHAZ region results in the formation of high-carbon martensite with maximum hardness (Ref. 21). On the other hand, the carbon content of the martensite in the FGHAZ is reduced relative to that of the CGHAZ due to the incomplete dissolution of carbides at the lower austenitizing temperatures reached in FGHAZ, and, hence, the hardness is lower.

Retained Austenite in Welds

In the regions of the single-pass weld that were submitted to the highest peak temperatures during the welding process (i.e., CGHAZ and FZ), thin continuous films of retained austenite were observed along PAG boundaries and lath boundaries.

This result agrees with previous ones since several authors have reported retained austenite with elongated film morphology along interlath boundaries. Thus, Shiue et al. (Ref. 22) investigated the influence of tempering treatments on retained austenite stability in Gr. 91 welds. The microstructure of the weld in the as-welded conditions was mainly comprised of lath martensite with retained austenite at martensite interlath boundaries; they postulated that the retained austenite was mechanically stabilized by welding residual stresses. In this sense, it is worth recalling that transformations (such as austenite to martensite) and thermal stresses are generally regarded as the two major components to raise residual stresses in welding hardenable steels. Film-like retained austenite was also observed by Hurtado-Noreña et al. (Ref. 23) in a P91 steel normalized at 1050°C for 30 min and air-cooled.

$M_{23}C_6$ Carbide Dissolution During Welding: Retained Austenite Presence vs. Ferrite Formation

The formation of austenite and the dissolution of carbides play important roles in the heat treatment of steels and have been carefully examined in previous literature; some of the results of that work may be useful to analyze the case of welding. Shtansky et al. (Ref. 24) have studied the mechanism of austenite formation along with the kinetics of carbide dissolution in a high alloy chromium steel (Fe-8.2Cr-0.2C) with $M_{23}C_6$ and M_7C_3 spheroidized carbides in ferrite as the initial structure. The austenite nucleation showed differences from that observed in low alloy steels in as much as austenite nucleated after a rather long incubation period between 2 s and 20 s at austenitizing temperatures as high as 850 to 900°C (1562 to 1652°F). After treating the alloy at 1000°C for 20 s, a ferrite shell around dissolving carbides within a martensite matrix was identified by TEM observations.

Yu et al. (Ref. 25) have reported thermal cycles designed to simulate the FGHAZ (peak temperature: 950°C [1742°F]; heating/cooling rates: 10°C [50°F]/s) of a Grade 91 steel. They found a partial dissolution of $M_{23}C_6$ precipitates using time-resolved x-ray diffraction (TRXRD) using synchrotron radiation and the formation of a small amount of ferrite on cooling by dilatometry. These authors proposed that precipitate dissolution may have enriched the local Cr and C content near the carbide-austenite interface, promoting ferrite formation, but they pointed out that the results were not conclusive to prove the hypothesis. In a later work, Yu (Ref. 26) added a simulation of $M_{23}C_6$ carbide dissolution and the ferrite formation phenomenon on cooling by thermodynamic and kinetic modeling using the Dictra software. The calculation of Cr composition profiles at 850, 949 (1740°F), and 950°C consistently pointed to ferrite formation due to partial dissolution of $M_{23}C_6$ that results in an accumulation of Cr at the carbide-austenite interface. Dictra simulations accompanied experimental welding cycles, again with a peak temperature of 950°C. At that temperature, TRXRD revealed an austenite matrix with a fraction of $M_{23}C_6$ carbides but no ferrite. By cooling to 700°C (1292°F), a small peak of ferrite

was observed, and the intensity of this peak increased as temperature decreased from 700 to 500°C (932°F).

As for the present study, if ferrite had been present around $M_{23}C_6$, it should have been identified by TEM; instead, our TEM observations revealed the presence of a retained austenite layer around the partially dissolved $M_{23}C_6$. Now, a small fraction of retained austenite in a component subjected to a welding process could imply microstructural heterogeneities at the subsequent tempering stage. Depending on the tempering temperature, retained austenite could decompose to non-tempered martensite (below 680°C [1256°F]) or right to ferrite (above 680°C) (Ref. 22). This means that a tempered matrix could include non-tempered or inhomogeneously tempered isolated regions, which in turn could alter the strength properties of the material (Ref. 27). The typical PWHT for P91 steels consists of tempering at 760°C (1400°F) for 4 h. Therefore, our results for single-pass welds indicated that the phase surrounding undissolved $M_{23}C_6$ carbides of the IC/FGHAZ before the conventional and nuclear power plant components enter service will be ferrite. The presence of ferrite soft phase around precipitates embedded in a hard matrix could be responsible for the creep cavities observed at the IC/FGHAZ close to A_{c3} due to the weak interface between them (Refs. 25, 28).

$M_{23}C_6$ Carbide Dissolution During Welding: Implications on the Relative Stability of MX Phases in Austenite

In 9–12% Cr tempered martensitic steels, including P91 steel, carbide-stabilized substructure strengthening is considered the most significant creep strengthening mechanism (Refs. 29, 30). Therefore, precipitate stability is a key factor both in the BM and in the HAZ of weldments. In a study of the austenitizing process of a P91 Nb steel, Signorelli et al. (Ref. 31) analyzed the evolution of precipitates present in samples held at 1050°C between 0 and 5 min by heating and cooling at 50°C (122°F)/s. They showed that all precipitates present in the as-received metallurgical state remained in the material at the very beginning of the 1050°C holding. Instead, $M_{23}C_6$ precipitates were not observed from the first minute of austenitization, and, interestingly, MX precipitates progressively changed their character from V-rich to Nb-rich.

Table 2 shows that in the present work, $M_{23}C_6$ precipitates were the major second phase identified from the BM to the intermediate FGHAZ and that VN was the major MX phase observed excepting the FGHAZ region near CGHAZ; in this zone, a higher fraction of NbCN precipitates was detected. These NbCN precipitates — a minor group in the BM — could nucleate and grow in the FGHAZ near the CGHAZ by combining the available Nb with C released by the dissolution of $M_{23}C_6$ precipitates. Another possibility is the destabilization of MX existing particles and the change of their chemical identity from VN to NbC for the same reason (i.e., C release to the austenite matrix). Thus, $M_{23}C_6$ carbide dissolution could play a critical role in defining the type of stable MX precipitate by altering the C/N ratio in a specific region of the HAZ. It has been reported that platelet type VN is stable rather than other MX with isotropic features for long-time exposure and long-term creep deformation (Ref. 5).

As for the Fe_3C carbide, identified in the HAZ and FZ, 9%Cr steel literature indicates that it is not stable at the peak temperatures reached during welding, which means that its appearance probably occurs by auto-tempering during cooling due to the high M_s values observed for low carbon steels (Ref. 32).

Conclusions

The microstructures of the heat-affected zone and fusion zone in the as-welded condition of a single-pass weld performed by the flux-cored arc welding process in a P91 steel have been characterized. The following are the major conclusions derived from the present work.

- The continuous increase in microhardness from base material to the fine-grained heat-affected zone is due to the increase in the fresh martensite fraction with increasing peak temperature. The slight change in microhardness from the FGHAZ to the FZ is associated with the increase in the C content of the matrix due to the dissolution of precipitates.

- All types of precipitates identified in the BM are present in the intercritical heat-affected zone, the FGHAZ near ICHAZ, and the intermediate FGHAZ. In the FGHAZ near the coarse-grained heat-affected zone, the dissolution of $M_{23}C_6$ led to precipitation of spherical NbCN. In the CGHAZ, Fe_3C and NbCN (P) were identified, and in the FZ, only Fe_3C precipitates were observed.

- In the CGHAZ and FZ, thin, continuous films of retained austenite were detected along the PAG and lath boundaries.

- Retained austenite was observed as a shell rounding some partially dissolved $M_{23}C_6$ carbides of the ICHAZ and FGHAZ after welding. This last result differs from previous observations that account for ferrite formation promoted by $M_{23}C_6$ carbide dissolution.

- MX precipitate identity and the presence of retained austenite for the ICHAZ and FGHAZ are potential factors to consider in the assessment of Type IV cracking susceptibility of welded joints in Grade 91 steels.

Acknowledgments

This work was partially supported by the National Agency of Scientific and Technological Promotion, Ministry of Science, Technology, and Productive Innovation of the Argentina Republic (grant PICT2019-2912). We would like to thank Dr. D. Vega for assistance with x-ray determinations.

References

1. Klueh, R. L. 2005. Elevated-temperature ferritic and martensitic steels and their application to future nuclear reactors. *International Materials Review* 50(5): 287–310. DOI: 10.1179/174328005X41140
2. Natesan, K., Majumdar, S., Shankar, P. S., and Shah, V. N. 2006. Preliminary materials selection issues for the next generation nuclear plant reactor pressure vessel. *Argonne National Laboratory, Report Number ANL/Ext-06-45*. DOI: 10.2172/9253283.
3. Vitek, J. M., and Klueh, R. L. 1983. Precipitation reactions during the heat treatment of ferritic steels. *Metallurgical Transactions A*. 14(6): 1047–1055. DOI: 10.1007/BF02670443
4. Kaneko, K., Matsumura, S., Sadakata, A., Fujita, K., Moon, W. J., Osaki, S., Nishimura, N., and Tomikiyo, Y. 2004. Characterization of

carbides at different boundaries of 9Cr-steel. *Materials Science and Engineering A* 374(1-2): 82–89. DOI: 10.1016/j.msea.2003.12.065

5. Yamada, K., Igarashi, M., Muneki, S., and Abe, F. 2001. Creep properties affected by morphology of MX in high-Cr ferritic steels. *ISIJ International* 41 (Supplement): S116–S120. DOI: 10.2355/isijinternational.41.Suppl_S116

6. Eggeler, G., Ramteke, A., Coleman, M., Chew, B., Hald, J., Jefeferay, C., Rantala, J., deWitte, M., and Mohrmann, R. 1994. Analysis of creep in a welded 'P91' pressure vessel. *International Journal of Pressure Vessels and Piping* 60(3): 237–257. DOI: 10.1016/0308-0161(94)90125-2

7. Cerjak, H., and Mayr, P. 2008. *Creep resistant steels*. Cambridge, England: Woodhead Publishing Limited.

8. Mayr, P. 2007. Weldability of modern 9%Cr steels for application in USC power plants. Ph.D. diss., Graz University of Technology, Graz, Austria.

9. Abson, D. J., and Rothwell, J. S. 2013. Review of type IV cracking of weldments in 9-12%Cr creep strength enhanced ferritic steels. *International Materials Reviews* 58(8): 437–473. DOI: 10.1179/1743280412Y.0000000016

10. Abe, F. 2000. R & D of advanced ferritic steels for 650°C USC boilers. *Proc. Int. Workshop on the innovative structural materials for infrastructure in 21st century*: 119–129. National Research Institute for Metals.

11. Vijayalakshmi, M., Saroja, S., Thomas Paul, V., Mythili, R., and Raghunathan, V. S. 1999. Microstructural zones in the primary solidification structure of weldment of 9Cr-1Mo steel. *Metallurgical and Materials Transactions A* 30A(1): 161–173. DOI: 10.1007/s11661-999-0204-8

12. Thomas Paul, V., Saroja, S., Hariharan, P., Rajadurai, A., and Vijayalakshmi, M. 2007. Identification of microstructural zones and thermal cycles in a weldment of modified 9Cr-1Mo steel. *Journal of Materials Science* 42(14): 5700–5713. DOI: 10.1007/s10853-006-0704-5

13. Sawada, K., Hara, T., Tabuchi, M., Kimura, K., and Kubushiro, K. 2015. Microstructure characterization of heat affected zone after welding in Mod.9Cr-1Mo steel. *Materials Characterization* 101: 106–113. DOI: 10.1016/j.matchar.2015.01.013

14. Wang, Y., Kannan, R., and Li, L. 2016. Characterization of as-welded microstructure of heat-affected zone in modified 9Cr-1Mo-V-Nb steel weldment. *Materials Characterization* 118(8): 225–234. DOI: 10.1016/j.matchar.2016.05.024

15. Luppo, M. I., Lionello, D. F., García de Andrés, C., and Danón, C. A., eds. G. Solórzano, and W. de Souza. 2010. Tempered and fresh martensite recognition using FEG-SEM in a T91 steel. *Proc. 17th International Microscopy Congress (IMC17)*.

16. Klueh, R. L., and Harries, D. R. 2001. High-chromium ferritic and martensitic steels for nuclear applications. *ASTM Monograph 3*, ASTM International.

17. Ennis, P. J., and Wachter, O. 1998. Investigation into the properties of the 9% chromium steel 9Cr-0.5Mo-1.8W-V-Nb with respect to its application as a pipe-work and boiler steel at elevated temperature: Part 2: Properties of weldments. *VGB PowerTech* 78: 84–94.

18. Marzocca, A. L., Luppo, M. I., and Zalazar, M. 2015. Identification of precipitates in weldments performed in an ASTM A335 Gr. P91 steel by the FCAW process. *Procedia Materials Science* 8: 894–903. DOI: 10.1016/j.mspro.2015.04.150

19. Jones, W. B., Hills, C. R., and Polonis, D. H. 1991. Microstructural evolution of modified 9Cr-1Mo Steel. *Metallurgical and Materials Transactions A* 22(5): 1049–1058. DOI: 10.1007/BF02661098

20. Anderson, P., Bellgart, T., and Jones, F. L. 2003 Creep deformation in a modified 9Cr-1Mo steel. *Materials Science and Technology* 19(2): 207–213. DOI: 10.1179/026708303225009436

21. Klueh, R. L., and Harries, D. R. 2001. *High-chromium ferritic and martensitic steels for nuclear applications*. ASTM Stock Number: MON03-EB. DOI: 10.1520/MON03-EB

22. Shiuie, R. K., Lan, K. C., and Chen, C. 2000. Toughness and austenite stability of modified 9Cr-1Mo welds after tempering. *Materials Science and Engineering A* 287(1): 10–16. DOI: 10.1016/S0921-5093(00)00831-5

23. Hurtado-Noreña, C., Danón, C. A., Luppo, M. I., and Bruzzoni, P. 2015. Evolution of minor phases in a 9PctCr steel: Effect of tempering temperature and relation with hydrogen trapping. *Metallurgical and Materials Transactions A* 46(9): 3972–3988. DOI: 10.1007/s11661-015-3045-7

24. Shtansky, D. V., Nakai, K., and Ohmori, Y. 1999. Formation of austenite and dissolution of carbides in Fe-8.2Cr-C alloys. *Zeitschrift für Metallkunde* 90(1): 1–37.

25. Yu, X., Babu, S. S., Terasaki, H., Komizo, Y., Yamamoto, Y., and Santella, M. L. 2013. Correlation of precipitate stability to increased creep resistance of Cr-Mo steel welds. *Acta Materialia* 61(6): 2194–2206. DOI: 10.1016/j.actamat.2012.12.040

26. Yu, X. 2015. Correlation of ferrite formation to creep properties of Cr-Mo steel welds. *Welding in the World* 59: 251–259. DOI: 10.1007/s40194-014-0200-5

27. Carrizo, D. A., Besoki, J. I., Luppo, M. I., Danón, C. A., and Ramos, C. P. 2019. Characterization of an ASTM A335 P91 ferritic-martensitic steel after continuous cooling cycles at moderate rates. *Journal of Materials Research and Technology* 8(1): 923–934. DOI: 10.1016/j.jmrt.2018.07.004

28. Albert, S. K., Matsui, M., Watanabe, T., Hongo, H., Kubo, K., and Tabuchi, M. 2002. Microstructural Investigation on Type IV cracking in a high Cr steel. *ISIJ International* 42(12): 1497–1504. DOI: 10.2355/isijinternational.42.1497

29. Eggeler, G., Nilsvang, N., and Ilschner, B. 1987. Microstructural changes in a 12% chromium steel during creep. *Steel Research* 58(2): 97–103. DOI: 10.1002/srin.198701594

30. Kostka, A., Tak, K. G., and Eggeler, G. 2008. On the effect of equal-channel angular pressing on creep of tempered martensite ferritic steels. *Materials Science and Engineering A* 481-482: 723–726. DOI: 10.1016/j.msea.2007.02.154

31. Signorelli, G. F., Danón, C. A., and Luppo, M. I. 2018. Study of the austenitization process in a P91 steel. *Proceeding of the International Conference on Fast Reactors and Related Fuel Cycles: Next Generation Nuclear Systems for Sustainable Development (FR17)*, IAEA – CN245–444, Vienna, Austria. ISBN: 978-92-0-108618-1.

32. Aborn, R. H. 1956. Low carbon martensites. *Transactions of American Society for Metals* 48: 51–57.

ANA LUCÍA MARZOCCA, CLAUDIO ARIEL DANÓN, and **MARÍA INÉS LUPPO** (luppo@ceia.gov.ar) are with the National Atomic Energy Commission, Materials Department, Buenos Aires, Argentina. **FLAVIO SOLDERA** is with the Saarland University, Department of Materials Science, Saarbrücken, Germany. **MÓNICA ZALAZAR** is with the National University of Comahue, Metallography and Welding Laboratory, Neuquén, Argentina.